

# Multigoal-oriented error estimation and mesh adaptivity for fluid-structure interaction

K. Ahuja<sup>1</sup>, B. Endtmayer<sup>2,3,5,6</sup>, M. C. Steinbach<sup>2</sup>, and T. Wick<sup>2,3,4</sup>

<sup>1</sup>Discipline of Computer Science and Engineering, Indian Institute of Technology Indore,  
Indore, India

<sup>2</sup>Leibniz Universität Hannover, Institut für Angewandte Mathematik, Welfengarten 1, 30167  
Hannover, Germany

<sup>3</sup>Cluster of Excellence PhoenixD (Photonics, Optics, and Engineering – Innovation Across  
Disciplines), Leibniz Universität Hannover, Germany

<sup>4</sup>Université Paris-Saclay, ENS Paris-Saclay, LMT – Laboratoire de Mécanique et Technologie,  
91190 Gif-sur-Yvette, France

<sup>5</sup> Johannes Kepler University Linz, Doctoral Program on Computational Mathematics,  
Altenbergerstr. 69, A-4040 Linz, Austria

<sup>6</sup>Austrian Academy of Sciences, Johann Radon Institute for Computational and Applied  
Mathematics, Altenbergerstr. 69, A-4040 Linz, Austria

## Abstract

In this work, we consider multigoal-oriented error estimation for stationary fluid-structure interaction. The problem is formulated within a variational-monolithic setting using arbitrary Lagrangian-Eulerian coordinates. Employing the dual-weighted residual method for goal-oriented a posteriori error estimation, adjoint sensitivities are required. For multigoal-oriented error estimation, a combined functional is formulated such that several quantities of interest are controlled simultaneously. As localization technique for mesh refinement we employ a partition-of-unity. Our algorithmic developments are substantiated with several numerical tests such as an elastic lid-driven cavity with two goal functionals, an elastic bar in a chamber with two goal functionals, and the FSI-1 benchmark with three goal functionals.

## 1 Introduction

This work is devoted to multigoal-oriented a posteriori error estimation and mesh adaptivity for the stationary fluid-structure interaction. Therein, the incompressible Navier-Stokes equations interact with elastic solids. References to extensive work on fluid-structure interaction include the textbooks [11, 30, 32, 10, 6, 8, 43, 31].

Multigoal-oriented a posteriori error estimation using the dual-weighted residual method [7, 5] with adjoint sensitivity measures goes back to Hartmann/Houston [35] and Hartmann [34]. The principal

idea is to construct a combined goal functional  $J_c$  as a linear combination of the individual goal functionals. The adjoint problem is then solved with respect to this combined goal functional.

In recent years, the multigoal-oriented error estimates have become very attractive as attested in several studies [40, 49, 39, 21]. Moreover, several improvements in the algorithmic techniques have been undertaken. In [25], the sign computation was facilitated such that only one additional problem of higher-order must be solved. Then, in [22], the error estimator was extended to balance the nonlinear iteration and the discretization error. For single goal functional this approach was first developed in [41]. Recently, two-sided error estimates could be proven under a saturation assumption [23]; a summary is contained in the PhD thesis of the second author [20]. Proofs for the saturation assumption are given in [16, 1]. For problems containing convection or transport, the assumption is not always true [23, Example 7.2]. This has consequences in this paper, since we consider again a system with convection terms in the Navier-Stokes part. Therefore, we cannot expect asymptotically perfect effectivity indices, but nonetheless the algorithms are reliable.

The objective in this paper is to apply the multigoal-oriented framework developed in [22] to fluid-structure interaction, which is a multidomain multiphysics problem. This is an illustrative example of a multiphysics problem in which various quantities in the different subdomains (flow and solid) might be controlled simultaneously. Specific interest is on drag, lift, pressure and displacement evaluations. Our model is based on the ALE (arbitrary Lagrangian-Eulerian) framework [15, 38, 28] using variational-monolithic coupling. Based on this monolithic model and combined goal functional, the Lagrangian is defined from which the primal model and the adjoint equation are derived. The resulting a posteriori error estimator is then localized using a partition-of-unity technique [46], which is specifically attractive for multidomain multiphysics problems, because the error estimator is directly based on the weak (variational) formulation without the traditional backward partial integration yielding that would yield second-order operators and interface terms to be evaluated. Consequently, the partition-of-unity is less error-prone as well as more efficient. Based on the localized error estimator, an adaptive scheme is derived from which error-controlled mesh adaptivity is carried out and for which two well-known numerical tests, the FSI-1 benchmark [37, 11, 10] and a modified lid-driven cavity example with elastic volume at the bottom [17, 18, 44] are taken to substantiate our algorithmic developments.

The outline of this paper is as follows. In Section 2 we formulate the primal problem and its Galerkin finite element discretization. In Section 3, multigoal-oriented error estimates are derived. Then, in Section 4 the errors are localized to carry out adaptive mesh refinement. In Section 5, three numerical tests are investigated in order to show the possibilities using our proposed multigoal-oriented framework. In the conclusions, our work is summarized.

## 2 Fluid-structure interaction: primal problem and discretization

In this section, we introduce the governing equations and formulate the adjoint problem. The latter is required for goal-oriented a posteriori error estimation with the dual-weighted residual (DWR) method [7].

## 2.1 Notation

We denote by  $\Omega \subset \mathbb{R}^d$ ,  $d = 2$ , the domain of the fluid-structure interaction problem. This domain consists of the subdomains  $\Omega_f$  and  $\Omega_s$ . The interface between both domains is denoted by  $\Gamma_i = \partial\Omega_f \cap \partial\Omega_s$ . The reference domains (obtained from a change of the coordinate system) are denoted by  $\hat{\Omega}_f$  and  $\hat{\Omega}_s$ , respectively, with the interface  $\hat{\Gamma}_i$ . Further, we denote the outer boundary with  $\partial\hat{\Omega} = \hat{\Gamma} = \hat{\Gamma}_D \cup \hat{\Gamma}_N$  where  $\hat{\Gamma}_D$  and  $\hat{\Gamma}_N$  denote Dirichlet and Neumann boundaries, respectively.

We adopt standard notation for the usual Lebesgue and Sobolev spaces [55]. We use the notation  $(\cdot, \cdot)$  for a scalar product on a Hilbert space  $X$  on the domain  $\Omega$  and  $\langle \cdot, \cdot \rangle$  for the scalar product on the boundary  $\partial\Omega$ . Finally, we introduce short hand notations for the Sobolev spaces:  $L := L^2(\Omega)$  and  $V := H^1(\Omega)$ , respectively  $\hat{L} := L^2(\hat{\Omega})$  and  $\hat{V} := H^1(\hat{\Omega})$ . If the fluid and solid domains must be distinguished, we add subscripts  $f$  or  $s$ . For Dirichlet boundaries  $\hat{\Gamma}_D$  with homogeneous conditions, we use  $V^0$  and  $\hat{V}^0$ , respectively.

## 2.2 Fluid flow in ALE coordinates

Let  $\hat{\mathcal{A}}_f: \hat{\Omega}_f \rightarrow \Omega_f$  be an invertible mapping, the so-called ALE transformation [15, 38, 28]. We define the unknowns  $\hat{v}_f$  and  $\hat{p}_f$  in  $\hat{\Omega}_f$  by

$$\hat{v}_f(\hat{x}) = v_f(x) = v_f(\hat{\mathcal{A}}_f(\hat{x})), \quad \hat{p}_f(\hat{x}) = p_f(x) = p_f(\hat{\mathcal{A}}_f(\hat{x})).$$

Then, with

$$\hat{F}_f := \hat{\nabla} \hat{\mathcal{A}}_f, \quad \hat{J}_f := \det(\hat{F}_f),$$

we obtain the relations

$$\nabla v_f = \hat{\nabla} \hat{v}_f \hat{F}_f^{-1}, \quad \int_{\Omega_f} f(x) dx = \int_{\hat{\Omega}_f} \hat{f}(\hat{x}) \hat{J}_f d\hat{x}.$$

With these relations, we can formulate the Navier-Stokes equations in artificial coordinates:

**Problem 2.1** (Variational fluid problem, ALE framework). *Let  $\hat{v}_f^D$  denote non-homogeneous flow Dirichlet boundary conditions. Find  $\{\hat{v}_f, \hat{p}_f\} \in \{\hat{v}_f^D + \hat{V}_f\} \times \hat{L}_f$ , such that*

$$\begin{aligned} (\hat{J}_f \hat{\rho}_f (\hat{F}_f^{-1} \hat{v}_f \cdot \hat{\nabla}) \hat{v}_f, \hat{\psi}^v)_{\hat{\Omega}_f} + (\hat{J}_f \hat{\sigma}_f \hat{F}_f^{-T}, \hat{\nabla} \hat{\psi}^v)_{\hat{\Omega}_f} - \langle \hat{g}_f, \hat{\psi}^v \rangle_{\hat{\Gamma}_i \cup \hat{\Gamma}_N} &= 0 \quad \forall \hat{\psi}^v \in \hat{V}_f^0, \\ (\widehat{\text{div}} (\hat{J}_f \hat{F}_f^{-1} \hat{v}_f), \hat{\psi}^p)_{\hat{\Omega}_f} &= 0 \quad \forall \hat{\psi}^p \in \hat{L}_f^0, \end{aligned}$$

with the ALE transformed Cauchy stress tensor

$$\hat{\sigma}_f := -\hat{p}_f I + \hat{\rho}_f \nu_f (\hat{\nabla} \hat{v}_f \hat{F}_f^{-1} + \hat{F}_f^{-T} \hat{\nabla} \hat{v}_f^T).$$

The viscosity and the density of the fluid are denoted by  $\nu_f$  and  $\hat{\rho}_f$ , respectively. The term  $I$  denotes the identity matrix in  $\mathbb{R}^{d \times d}$ . The function  $\hat{g}_f$  represents Neumann boundary conditions for both physical boundaries (e.g., stress zero at outflow boundary), and normal stresses on  $\hat{\Gamma}_i$ . We note that the specific choice of the transformation  $\hat{\mathcal{A}}_f$  is up to now arbitrary and left open.

### 2.3 Solid description in Lagrangian coordinates

Solids are usually formulated in Lagrangian coordinates, which means that one needs to find a mapping from the physical (deformed) domain  $\Omega_s$  to the reference domain  $\hat{\Omega}_s$ .

The transformation  $\hat{\mathcal{A}}_s: \hat{\Omega}_s \rightarrow \Omega_s$  is naturally given by the deformation itself:

$$\hat{\mathcal{A}}_s(\hat{x}) = \hat{x} + \hat{u}_s(\hat{x}), \quad \hat{F}_s := \hat{\nabla} \hat{\mathcal{A}}_s = I + \hat{\nabla} \hat{u}_s, \quad \hat{J}_s := \det(\hat{F}_s). \quad (1)$$

This transformation is identical in its definition to the ALE transformation  $\hat{\mathcal{A}}_f$ , and for this reason both can be identified by omitting the subscripts  $f$  and  $s$ .

As material law, we work with the elastic compressible (geometrically) nonlinear Saint Venant-Kirchhoff material (STVK). It is well suited for (relatively) large displacements with the limitation of small strains. The strain is defined by  $\hat{E} := \frac{1}{2}(\hat{F}^T \hat{F} - I)$ . The sought physical unknowns are the displacement  $\hat{u}$  and the velocity  $\hat{v}$ :

**Problem 2.2** (Solid in Lagrangian coordinates). *Find  $\hat{u}_s \in \hat{V}_s^0$  such that*

$$(\hat{J}_s \hat{\sigma}_s \hat{F}_s^{-T}, \hat{\nabla} \hat{\psi}^v)_{\hat{\Omega}_s} - \langle \hat{J}_s \hat{\sigma}_s \hat{F}_s^{-T} \hat{n}_s, \hat{\psi}^v \rangle_{\hat{\Gamma}_i \cup \hat{\Gamma}_N} = (\hat{\rho}_s \hat{f}_s, \hat{\psi}^v)_{\hat{\Omega}_s} \quad \forall \hat{\psi}^v \in \hat{V}_s^0, \quad (2)$$

where  $\hat{n}_s$  is the outer normal vector on  $\hat{\Gamma}_i$  and  $\hat{\Gamma}_N$ , respectively. The Cauchy stress tensors for STVK material is given by

$$\hat{\sigma}_s := \hat{J}^{-1} \hat{F} (\lambda_s (\text{tr} \hat{E}) I + 2\mu_s \hat{E}) \hat{F}^T \quad (3)$$

with the positive Lamé coefficients  $\mu_s$  and  $\lambda_s$ . External volume forces are described by the term  $\hat{f}_s$ .

### 2.4 The coupled problem in ALE coordinates

In the solid part,  $\hat{\mathcal{A}}_s$  is determined naturally by the solid displacements (see for example [13]). Therefore, only the flow part  $\hat{\mathcal{A}}_f$  needs to be specified. On the interface  $\hat{\Gamma}_i$ , this transformation is given by taking the solid displacement  $\hat{u}_f = \hat{u}_s$  such that we can define

$$\hat{\mathcal{A}}_f(\hat{x})|_{\hat{\Gamma}_i} := \hat{x} + \hat{u}_s(\hat{x})|_{\hat{\Gamma}_i}. \quad (4)$$

On the outer boundary of the fluid domain,  $\partial \hat{\Omega}_f \setminus \hat{\Gamma}_i$ , there holds  $\hat{\mathcal{A}}_f = \text{id}$ . Inside  $\hat{\Omega}_f$ , the transformation should be sufficiently smooth and regular. For some relevant mathematical regularity results, we refer to [28, 29]. Away from the interface  $\hat{\Gamma}_i$  the mapping can be extended arbitrarily in various fashions, for example harmonic, nonlinear harmonic/elastic [48], or biharmonic [51], to mention just a few cases. Some recent results on mesh motion can be found in [47]. The simplest harmonic model reads (in strong formulation):

**Problem 2.3** (Harmonic mesh motion). *Find  $\hat{u}_f: \hat{\Omega}_f \rightarrow \mathbb{R}^d$  such that*

$$\widehat{\text{div}}(\hat{\sigma}_g) = 0, \quad \hat{u}_f = \hat{u}_s \text{ on } \hat{\Gamma}_i, \quad \hat{u}_f = 0 \text{ on } \partial \hat{\Omega}_f \setminus \hat{\Gamma}_i, \quad (5)$$

with  $\hat{\sigma}_g = \hat{\alpha}_u \hat{\nabla} \hat{u}_f$  and  $\hat{\alpha}_u > 0$ .

In the following, we focus on a variational-monolithic description of the coupled problem [43, 53]. To this end, we define a continuous variable  $\hat{u}$  in  $\hat{\Omega}$  defining the deformation in  $\hat{\Omega}_s$  and supporting the transformation in  $\hat{\Omega}_f$ . Thus, we drop subscripts on  $\hat{u}$ , and because the definition of  $\hat{\mathcal{A}}_f$  coincides with the previous definition of  $\hat{\mathcal{A}}_s$ , we define in  $\hat{\Omega}$ :

$$\hat{A} := \text{id} + \hat{u}, \quad \hat{F} := I + \hat{\nabla} \hat{u}, \quad \hat{J} := \det(\hat{F}). \quad (6)$$

Then, we obtain the overall problem formulation:

**Problem 2.4** (Variational-monolithic fluid-structure interaction framework).

Find  $\{\hat{v}, \hat{u}, \hat{p}\} \in \{\hat{v}^D + \hat{V}\} \times \hat{V} \times \hat{L}$  such that

$$\begin{aligned} & (\hat{\rho}_f \hat{J} (\hat{F}^{-1} \hat{v} \cdot \hat{\nabla}) \hat{v}), \hat{\psi}^v)_{\hat{\Omega}_f} + (\hat{J} \hat{\sigma}_f \hat{F}^{-T}, \hat{\nabla} \hat{\psi}^v)_{\hat{\Omega}_f} + (\hat{J} \hat{\sigma}_s \hat{F}^{-T}, \hat{\nabla} \hat{\psi}^v)_{\hat{\Omega}_s} \\ & - \langle \hat{g}, \hat{\psi}^v \rangle_{\hat{\Gamma}_N} - (\hat{\rho}_f \hat{J} \hat{f}_f, \hat{\psi}^v)_{\hat{\Omega}_f} - (\hat{\rho}_s \hat{f}_s, \hat{\psi}^v)_{\hat{\Omega}_s} = 0 \quad \forall \hat{\psi}^v \in \hat{V}^0, \\ & (\hat{v}, \hat{\psi}^u)_{\hat{\Omega}_s} + (\hat{\sigma}_g, \hat{\nabla} \hat{\psi}^u)_{\hat{\Omega}_f} = 0 \quad \forall \hat{\psi}^u \in \hat{V}^0, \\ & (\widehat{\text{div}} (\hat{J} \hat{F}^{-1} \hat{v}_f), \hat{\psi}^p)_{\hat{\Omega}_f} = 0 \quad \forall \hat{\psi}^p \in \hat{L}, \end{aligned}$$

with  $\hat{\rho}_f, \nu_f, \mu_s, \lambda_s, \hat{F}$ , and  $\hat{J}$ . The stress tensors  $\hat{\sigma}_f, \hat{\sigma}_s$ , and  $\hat{\sigma}_g$  are defined in Problems 2.1, 2.2, and 2.3, respectively. Written in an abstract form, we have: find  $\hat{U} \in \hat{X} := \{\hat{v}^D + \hat{V}\} \times \hat{V} \times \hat{L}$  such that

$$\hat{A}(\hat{U})(\hat{\Psi}) = 0 \quad \forall \hat{\Psi} \in \hat{X}^0,$$

where  $\hat{X}^0 := \hat{V}^0 \times \hat{V}^0 \times \hat{L}$ , and where the semi-linear form  $\hat{A}(\hat{U})(\hat{\Psi})$  is nonlinear in  $\hat{U}$  and linear in the test function  $\hat{\Psi}$ .

## 2.5 Galerkin finite element discretization

We assume that  $\Omega \subset \mathbb{R}^d$  is a polyhedral domain. Let  $\mathcal{T}_h$  be a subdivision of  $\Omega$  into quadrilateral elements such that  $\bigcup_{K \in \mathcal{T}_h} \bar{K} = \bar{\Omega}$  and  $K \cap K' = \emptyset$  for all  $K, K' \in \mathcal{T}_h$  with  $K \neq K'$ . The discretization parameter is denoted by  $h$ .

Working with adaptive meshes, to ensure global continuity and therefore global conformity, the degrees of freedom on interfaces between different elements of different refinement levels have to fulfill additional constraints. These are obtained by interpolation where hanging nodes [12] do not carry any degrees of freedom. Specifically, we use continuous tensor-product finite elements as described in [14] and [9].

Using such a conforming method, we have  $\hat{X}_h \subset \hat{X}$ , where  $\hat{X}_h$  denotes the finite-dimensional space. This space is composed of the subspaces  $\hat{V}_h$  and  $\hat{W}_h$  for the unknowns  $\hat{v}_h$  and  $\hat{p}_h$ , respectively. To satisfy discrete inf-sup stability (also known as LBB condition), we must choose the discrete function spaces in a proper way. To this end, we work with the well-known Taylor-Hood element  $Q_c^2/Q_c^1$  using biquadratic functions for the velocities and bilinear functions for the pressure.

The resulting discrete primal problem reads as follows in a compact abstract notation: find  $\hat{U}_h \in \hat{X}_h$  such that

$$\hat{A}(\hat{U}_h)(\hat{\Psi}_h) = 0 \quad \forall \hat{\Psi}_h \in \hat{X}_h^0. \quad (7)$$

### 3 Multigoal-oriented a posteriori error estimation

In this section, we describe multigoal-oriented error estimation with the dual-weighted residual method. For examples of goal-oriented error estimation in fluid-structure interaction we refer the reader to [50, 27, 42, 33, 17, 19, 43, 26] and [54] including an open-source github version for single goal functionals.

#### 3.1 Optimization problem

Goal-oriented error estimation aims at controlling the discretization error between the continuous solution  $\hat{U} \in \hat{X}$  and the discrete solution  $\hat{U}_h \in \hat{X}_h$  measured in terms of a goal functional  $J: \hat{X} \rightarrow \mathbb{R}$ . Such goal functionals describe technical quantities of interest such as drag or lift values, or point evaluations, but also include global norm errors.

In order to derive sensitivity information, the evaluation of  $J(\hat{U})$  is artificially reformulated as an optimization problem where the constraint already determines  $\hat{U}$  uniquely [7],

$$\min J(\hat{U}) \quad \text{s.t.} \quad \hat{A}(\hat{U})(\hat{\Psi}) = 0 \quad \forall \hat{\Psi} \in \hat{X}.$$

The Lagrangian reads

$$L(\hat{U}, \hat{Z}) = J(\hat{U}) - \hat{A}(\hat{U})(\hat{Z}).$$

As usual, the solution  $\hat{U}$  of the above optimization problem is characterized by the existence of an adjoint (or dual) solution  $\hat{Z} \in \hat{X}$  that satisfies the first-order necessary conditions

$$\begin{aligned} 0 = L'_U(\hat{U}, \hat{Z})(\hat{\Phi}) &= J'(\hat{U})(\hat{\Phi}) - \hat{A}'(\hat{U})(\hat{\Phi}, \hat{Z}) & \forall \hat{\Phi} \in \hat{X}, \\ 0 = L'_Z(\hat{U}, \hat{Z})(\hat{\Psi}) &= -\hat{A}(\hat{U})(\hat{\Psi}) & \forall \hat{\Psi} \in \hat{X}. \end{aligned}$$

The second condition is the given primal problem. The first condition is the so-called adjoint problem. The derivatives  $\hat{A}'(\hat{U})$  and  $J'(\hat{U})$  are understood in the Fréchet-sense of the nonlinear operator or functional, respectively, evaluated at the point  $\hat{U}$ .

#### 3.2 Adjoint problem

From the previous optimality system, we see that the adjoint problem reads: find  $Z \in X^0$  such that

$$\hat{A}'(\hat{U})(\hat{\Phi}, \hat{Z}) = J'(\hat{U})(\hat{\Phi}) \quad \forall \hat{\Phi} \in \hat{X}^0. \quad (8)$$

We notice that the adjoint problem is always linear, but the nonlinear state variable  $\hat{U}$  enters.

**Problem 3.1** (Adjoint problem for stationary fluid-structure interaction). *Find  $\hat{Z} \in \hat{X}^0$  such that*

$$\begin{aligned}
\hat{A}'(\hat{U})(\hat{\Psi}, \hat{Z}) &= \hat{\rho}_f (\hat{\nabla} \hat{\psi}^v \hat{J} \hat{F}^{-1} \hat{v}_f + \hat{\nabla} \hat{v}_f \hat{J} \hat{F}^{-1} \hat{\psi}^v, \hat{z}_f^v)_{\hat{\Omega}_f} + \hat{\rho}_f (\hat{\nabla} \hat{v}_f [\hat{J} \hat{F}^{-1}]'(\hat{\psi}^u) \hat{v}_f, \hat{z}_f^v)_{\hat{\Omega}_f} \\
&+ (\hat{\rho}_f \nu_f (\hat{\nabla} \hat{\psi}^v \hat{F}^{-1} + \hat{F}^{-T} (\hat{\nabla} \hat{\psi}^v)^T) \hat{J} \hat{F}^{-T}, \hat{\nabla} \hat{z}_f^v)_{\hat{\Omega}_f} \\
&+ (\hat{\rho}_f \nu_f (\hat{\nabla} \hat{v}_f [\hat{F}^{-1}]'(\hat{\psi}^u) + [\hat{F}^{-T}]'(\hat{\psi}^u) \hat{\nabla} \hat{v}_f^T) \hat{J} \hat{F}^{-T}, \hat{\nabla} \hat{z}_f^v)_{\hat{\Omega}_f} - (\hat{\psi}^p \hat{J} \hat{F}^{-T}, \hat{\nabla} \hat{z}_f^v)_{\hat{\Omega}_f} \\
&+ (\hat{\rho}_f \nu_f (\hat{\nabla} \hat{v}_f \hat{F}^{-1} + \hat{F}^{-T} \hat{\nabla} \hat{v}_f^T) [\hat{J} \hat{F}^{-T}]'(\hat{\psi}^u), \hat{\nabla} \hat{z}_f^v)_{\hat{\Omega}_f} - (\hat{\rho}_f [\hat{J} \hat{F}^{-T}]'(\hat{\psi}^u), \hat{\nabla} \hat{z}_f^v)_{\hat{\Omega}_f} \\
&+ (\lambda_s (\text{tr} \hat{E}'(\hat{\psi}^u) \hat{F} + \text{tr} \hat{E} \hat{F}'(\hat{\psi}^u)) + 2\mu_s (\hat{F}'(\hat{\psi}^u) \hat{E} + \hat{F} \hat{E}'(\hat{\psi}^u)), \hat{\nabla} \hat{z}_s^v)_{\hat{\Omega}_s} \\
&- (\hat{\psi}^v, \hat{z}_s^u)_{\hat{\Omega}_s} + (\alpha_u \hat{\nabla} \hat{\psi}^u, \hat{\nabla} \hat{z}_f^u)_{\hat{\Omega}_f} + (\hat{\partial}_1 \hat{\psi}^{v1} + \hat{\partial}_2 \hat{\psi}^{v2}, \hat{z}_f^p)_{\hat{\Omega}_f} \\
&+ (\hat{\partial}_2 \hat{\psi}^{u1} \hat{\partial}_1 \hat{v}_{f,1} - \hat{\partial}_2 \hat{\psi}^{u2} \hat{\partial}_1 \hat{v}_{f,2} - \hat{\partial}_1 \hat{\psi}^{u2} \hat{\partial}_2 \hat{v}_{f,1} + \hat{\partial}_1 \hat{\psi}^{u1} \hat{\partial}_{f,2} \hat{v}_2, \hat{z}_f^p)_{\hat{\Omega}_f} \\
&= J'(\hat{U})(\hat{\Psi}) \quad \forall \hat{\Psi} \in \hat{X}^0.
\end{aligned}$$

### 3.3 Discrete adjoint problem

The corresponding discrete adjoint problem reads as follows: find  $Z_h \in X_h$  corresponding to  $U_h \in X_h$  such that

$$\hat{A}'(\hat{U}_h)(\hat{\Phi}_h, \hat{Z}_h) = J'(\hat{U}_h)(\hat{\Phi}_h) \quad \forall \hat{\Phi}_h \in \hat{X}_h, \quad (9)$$

where  $\hat{U}_h$  solves the discrete primal problem. Clearly the solution  $\hat{Z}_h$  depends on  $\hat{U}_h$ . Algorithmically, we will first compute the primal solution  $\hat{U}_h$  and then enter into the adjoint problem [7]. Note that due to Galerkin orthogonality, the error estimator stated below will always yield a zero error unless the adjoint solution contains higher-order information (see [7]). Here, we simply use a globally higher-order finite element solution. To this end, the adjoint velocities and displacements are approximated by  $Q_c^4$  functions and the pressures by  $Q_c^2$  functions.

### 3.4 A posteriori error estimators

In the previous sections, we explained the derivation and discretization of both the primal and adjoint problems. Using the main theorem from [7], we obtain the following error identity, which serves as basis for a posteriori error control.

**Theorem 3.2.** *We have the error identity*

$$J(\hat{U}) - J(\hat{U}_h) = \frac{1}{2} \rho(\hat{U}_h)(\hat{Z} - \hat{\Phi}_h) + \frac{1}{2} \rho^*(\hat{U}_h, \hat{Z}_h)(\hat{U} - \hat{\Psi}_h) + \mathcal{R}_h^{(3)} \quad \forall \{\hat{\Psi}_h, \hat{\Phi}_h\} \in \hat{X}_h \times \hat{X}_h, \quad (10)$$

where the first two terms on the right-hand side are given by the primal and adjoint residuals:

$$\begin{aligned}
\rho(\hat{U}_h)(\hat{Z} - \hat{\Phi}_h) &:= -A(\hat{U}_h)(\hat{Z} - \hat{\Phi}_h), \\
\rho^*(\hat{U}_h, \hat{Z}_h)(\hat{U} - \hat{\Psi}_h) &:= J'(\hat{U}_h)(\hat{U} - \hat{\Psi}_h) - A'(\hat{U}_h)(\hat{U} - \hat{\Psi}_h, \hat{Z}_h).
\end{aligned}$$

The remainder term  $\mathcal{R}_h^{(3)}$  is of cubic order. The arguments  $(\hat{Z} - \hat{\Phi}_h)$  and  $(\hat{U} - \hat{\Psi}_h)$  can be obtained by interpolation differences, i.e.,  $(\hat{Z} - i_a \hat{Z})$  and  $(\hat{U} - i_p \hat{U})$ , respectively, where  $i_a: \hat{X}_h^{\text{high}} \rightarrow \hat{X}_h$  and  $i_p: \hat{X}_h^{\text{high}} \rightarrow \hat{X}_h$  are interpolations from higher order finite element spaces to low-order spaces; see also Section 3.3.

*Proof.* We refer the reader to [7, 41, 23]. □

**Corollary 3.3** (Error estimator based on primal residual). *The primal error identity reads:*

$$J(\hat{U}) - J(\hat{U}_h) = \rho(\hat{U}_h)(\hat{Z} - \hat{\Phi}_h) + \mathcal{R}_h^{(2)}, \quad (11)$$

where the remainder term is now of second order.

The previous error identity can be used to define the error estimator  $\eta$ , which can be further utilized to design adaptive schemes. Therein, we propose practical error estimators in which all information can be computed and remainder terms are neglected.

**Definition 3.4** (Practical error estimators). *A practical error estimator for the goal functional  $J(\hat{U})$  reads:*

$$\eta_h := \frac{1}{2}\rho(\hat{U}_h)(\hat{Z}_h - i_a\hat{Z}_h) + \frac{1}{2}\rho^*(\hat{U}_h, \hat{Z}_h)(\hat{U}_h - i_p\hat{U}_h). \quad (12)$$

*A purely primal and hence less accurate, but cheaper, practical error estimator reads:*

$$\eta_h := \frac{1}{2}\rho(\hat{U}_h)(\hat{Z}_h - i_a\hat{Z}_h). \quad (13)$$

*The primal error part has a remainder term of only second order (see Corollary 3.3), but is cheaper because only the adjoint solution needs to contain higher order information for the interpolation  $i_a$ . In (12) both the primal and the adjoint must contain higher order information for  $i_a$  and  $i_p$ , which is of course expensive in terms of the computational cost.*

### 3.5 Multiple goal functionals

The error estimation is now extended to multiple goal functionals. Assume that we are given  $N$  goal functionals  $J_i$ ,  $i = 1, \dots, N$ . In a flow problem this might be drag and lift as well as estimates of the pressure and some solid displacement of the elastic structure. In this case, we would have  $N = 4$ .

We construct an overall goal functional  $J_c$  as a convex combination of the individual goal functionals, with weights  $\omega_i \geq 0$  that sum up to one and signs  $\sigma_i \in \{-1, +1\}$ :

$$J_c(\hat{\Phi}) := \sum_{i=1}^N \omega_i \sigma_i J_i(\hat{\Phi}), \quad \hat{\Phi} \in \hat{X}. \quad (14)$$

Here the choice of  $\sigma_i$  is a crucial aspect since all terms in the sum should have the same sign to avoid cancellation. As we need to compute  $|J_c(\hat{U}) - J_c(\hat{U}_h)|$ , we follow previous studies and use

$$\sigma_i := \text{sign}(J_i(\hat{U}) - J_i(\hat{U}_h)). \quad (15)$$

Later, in Section 5, we set

$$w_i := \omega_i \sigma_i.$$

We notice that a relative combined functional may be defined with  $w_i := \omega_i \frac{\sigma_i}{|J_i(\hat{U}_h)|}$ , which is however not employed in this work. Some computations studying the influence of different weights  $\omega_i$  are conducted in Section 5.



A first sign computation was proposed in [35] and later extended to a more efficient way in [25]. In practice  $J_c$  from (14) is now used as right hand side in the adjoint problems (8) and (9), respectively. We notice that for nonlinear goal functionals, we need the Fréchet derivative of the combined functional  $J_c$  (14); for technical details, we refer to [22].

**Definition 3.5** (Combined functional error estimators). *A practical error estimator for the combined goal functional  $J_c(\hat{U})$  reads:*

$$J_c(\hat{U}) - J_c(\hat{U}_h) \approx \eta_h := \frac{1}{2}\rho(\hat{U}_h)(\hat{Z}_h - i_a \hat{Z}_h) + \frac{1}{2}\rho^*(\hat{U}_h, \hat{Z}_h)(\hat{U}_h - i_p \hat{U}_h). \quad (16)$$

As above, a purely primal and less accurate but cheaper practical error estimator reads:

$$J_c(\hat{U}) - J_c(\hat{U}_h) \approx \eta_h := \frac{1}{2}\rho(\hat{U}_h)(\hat{Z}_h - i_a \hat{Z}_h). \quad (17)$$

In both cases the primal problem is computed as for a single goal functional, and in the adjoint problem the combined goal functional  $J_c$  (including sign computation) is employed.

## 4 Error localization and adaptive algorithms

### 4.1 Localization

For the localization of the error estimator to single DoFs or elements, we use the partition-of-unity (PU) technique as suggested in [46]. To this end, we choose a set of finite element basis functions  $\hat{V}_{PU} := \{\hat{\psi}_1, \dots, \hat{\psi}_M\}$  with  $\dim \hat{V}_{PU} = M$  such that  $\sum_{i=1}^M \psi_i \equiv 1$ . These functions can be low-order scalar-valued bilinear shape functions  $Q_1^c$ . We then distribute  $\eta_i$  to the corresponding elements with certain weights as explained in [22, 20]. Inserting this into (17), we obtain

**Proposition 4.1.** *For the combined goal functional  $J_c$ , using the primal error part  $\rho(\hat{U}_h)(\cdot)$ , we have the a posteriori error estimate*

$$|J_c(\hat{U}) - J_c(\hat{U}_h)| \leq |\eta_h| := \left| \sum_{i=1}^M \eta_i \right| \leq \sum_{i=1}^M |\eta_i| \quad (18)$$

with the PU-DoF indicators

$$\begin{aligned} \eta_i &= -A(\hat{U}_h)((\hat{Z}_h - i_a \hat{Z}_h)\hat{\Psi}_i) \\ &= -(\hat{\rho}_f \hat{J}(\hat{F}^{-1} \hat{v}_f \cdot \hat{\nabla}) \hat{v}_f), \hat{\psi}_i^v)_{\hat{\Omega}_f} - (\hat{J} \hat{\sigma}_f \hat{F}^{-T}, \hat{\nabla} \hat{\psi}_i^v)_{\hat{\Omega}_f} + \langle \hat{g}_f, \hat{\psi}_i^v \rangle_{\hat{\Gamma}_N} \\ &\quad - (\hat{F} \hat{\Sigma}, \hat{\nabla} \hat{\psi}_i^v)_{\hat{\Omega}_s} - (\hat{\sigma}_{\text{mesh}}, \hat{\nabla} \hat{\psi}_i^u)_{\hat{\Omega}_f} - (\widehat{\text{div}}(\hat{J} \hat{F}^{-1} \hat{v}_f), \hat{\psi}_i^p)_{\hat{\Omega}_f} + (\hat{J} \hat{f}_f, \hat{\psi}_i^v) + (\hat{f}_s, \hat{\psi}_i^v). \end{aligned}$$

Here the weighting functions are defined with the interpolation  $i_a: \hat{X}_h^{\text{high}} \rightarrow \hat{X}_h$  as

$$\hat{\psi}_i^v := (\hat{z}_{h,v}^{\text{high}} - \hat{z}_{h,v})\psi_i, \quad \hat{\psi}_i^u := (\hat{z}_{h,u}^{\text{high}} - \hat{z}_{h,u})\psi_i, \quad \hat{\psi}_i^p := (\hat{z}_{h,p}^{\text{high}} - \hat{z}_{h,p})\psi_i.$$

To measure the quality of the proposed error estimator, we consult the effectivity index [4] and indicator index [46], respectively:

$$I_{\text{eff}} := \frac{|\eta_h|}{|J_c(\hat{U}) - J_c(\hat{U}_h)|}, \quad I_{\text{ind}} := \frac{\sum_i |\eta_i|}{|J_c(\hat{U}) - J_c(\hat{U}_h)|}. \quad (19)$$

## 4.2 Adaptive algorithm

1. Compute the primal solution  $\hat{U}_h \in \hat{X}_h$  on the mesh  $\mathcal{T}_l$ , where  $l \in \mathbb{N}$  is the current mesh level.
2. Construct the combined goal functional  $J_c$  via (14).
3. Solve (9) on the mesh  $\mathcal{T}_l$  with  $J_c$  as right hand side and obtain (high-order)  $\hat{Z}_h \in \hat{X}_h^{\text{high}}$ .
4. Evaluate  $|\eta| := |\sum_i \eta_i|$  in (18).
5. If the stopping criterion is satisfied,  $|J_c(\hat{U}) - J_c(\hat{U}_h)| \leq |\eta| \leq TOL$ , then accept  $U_h$  within the tolerance  $TOL$ . Otherwise, proceed to the following step.
6. Mark all elements  $K_i$  for refinement that touch DoFs  $i$  whose indicator  $\eta_i$  satisfies  $\eta_i \geq \frac{\alpha\eta}{M_{\text{el}}}$  (where  $M_{\text{el}}$  denotes the total number of elements of the mesh  $\mathcal{T}_h$  and  $\alpha \approx 1$ ).
7. Refine all marked elements to obtain the mesh  $\mathcal{T}_{l+1}$ .
8. Go to Step 1.

## 5 Numerical tests

In this section, we present three numerical tests: an elastic lid-driven cavity with two goal functionals, an elastic bar in a chamber with two goal functionals, and the FSI-1 benchmark with three goal functionals. The implementation is based on the open-source finite element library deal.II [2, 3] and extensions of our own fluid-structure code publications [52, 54] towards multigoal-oriented error estimation from [20]. In all examples, we work with the primal error estimator from Proposition 4.1.

### 5.1 Example 1: lid-driven cavity with elastic volume at bottom

This first configuration is a well-known example in computational fluid dynamics and was extended to fluid-structure interaction in [17] where an elastic bottom is added in the lower part of the domain.

**Configuration** The computational domain is  $\Omega = (0, 2)^2$  with flow in  $\Omega_f = [0, 2] \times [0.5, 2]$  and the solid domain  $\Omega_s = [0, 2] \times [0, 0.5]$ .

**Boundary conditions** On the top boundary  $\hat{\Gamma}_{\text{top}} = \{2\} \times [0, 2]$ , we prescribe overflow:

$$v_0 = 0.5 \times \begin{cases} \sin^2(\pi x/0.6), & x \in [0.0, 0.3], \\ 1, & x \in (0.3, 1.7), \\ \sin^2(\pi(x - 2.0)/0.6), & x \in [1.7, 2.0]. \end{cases}$$

On the other boundaries, we use homogeneous Dirichlet conditions, i.e.,  $\hat{v} = 0$  on  $\partial\hat{\Omega} \setminus \hat{\Gamma}_{\text{top}}$ . Moreover,  $\hat{u} = 0$  on  $\partial\hat{\Omega}$  and  $\partial_n p = 0$  on  $\partial\hat{\Omega}$ . We notice that, because of the pressure boundary conditions, the pressure is not unique and must be constrained.

**Parameters** For the fluid we use the density  $\varrho_f = 1.0 \text{ kgm}^{-3}$  and kinematic viscosity  $\nu_f = 0.2 \text{ m}^2\text{s}^{-1}$ . The elastic solid is characterized by the density  $\varrho_s = 1.0 \text{ kgm}^{-3}$  and Poisson's ratio  $\nu_s = 0.4$ . Furthermore, we use the Lamé coefficient  $\mu_s = 2.0 \text{ kgm}^{-1}\text{s}^{-2}$ .

**Quantities of interest and goals** In this example, we construct the following combined functional:

$$J_c(\hat{U}) = w_1 J_{\text{drag}}(\hat{U}) + w_2 J_2(\hat{u}),$$

with the weights  $w_1, w_2 \in \mathbb{R}$  and  $w_1 = w_2 = 0.5$  (see (14)) and  $J_{\text{drag}}(\hat{U})$  (see definition below (21)) and  $J_2(\hat{u}) := \hat{u}(1.5, 0.25)$ . The individual reference values are computed on a sufficiently refined mesh:

$$\begin{aligned} J_{\text{drag}}(\hat{U}) &= -9.35437 \times 10^{-2}, \\ J_2(\hat{U}) &= -4.68984 \times 10^{-3}. \end{aligned}$$

The combined reference value is then obtained as

$$J_c(\hat{U}) = \omega_1 J_{\text{drag}}(\hat{U}) + \omega_2 J_2(\hat{u}). \quad (20)$$

**Results and discussion** The original geometry is once uniformly refined and serves as initial mesh. Then we perform six adaptive refinements. The final two goal functionals and the combined functional values are provided in Table 1. We see that the values do not necessarily need to be positive.

Drag	$-9.355 \times 10^{-2}$
Pressure	$-4.688 \times 10^{-3}$
$J_c$	$-4.912 \times 10^{-2}$

Table 1: Example 1: Final values of goal functionals for  $\omega_1 = \omega_2 = 0.5$ , where  $J_c$  is obtained with the help of (20).

As we observe in Table 2, the estimated error  $\eta_h$  of  $J_c$  drops down to  $1.71 \times 10^{-6}$ . The effectivity indices  $I_{\text{eff}}$  perform relatively well being close to 1 on the last three meshes. The slight deviation can be explained by the nonlinear, coupled problem and by utilizing only the primal error part. In a comparison with uniform mesh refinement, we observe that the true error behaves first slightly worse than adaptive mesh refinement, but finally better. However the computational cost measured in terms of the degrees of freedom is much higher for uniform mesh refinement. The estimators behave similarly at each refinement level, but for different degrees of freedom. These results clearly show that adaptive mesh refinement is an efficient procedure. Table 3 shows the effect of choosing different weights  $\omega_1, \omega_2$ . Therein, always the above reference value for  $J_c(\hat{U})$  is used. For the case  $\omega_1 = 0.00$  and  $\omega_2 = 1.00$  all values vanish. The reason is that our point evaluation is a grid point and therefore the values vanish if we use interpolation. A more detailed explanation for this phenomena and solutions to overcome this problem are found in [24].

Dofs	$ J_c(\hat{U}) - J_c(\hat{U}_h) $	$ \eta_h $	$\sum_i  \eta_i $	$I_{\text{eff}}$	$I_{\text{ind}}$
195	$8.80 \times 10^{-4}$	$1.81 \times 10^{-3}$	$9.96 \times 10^{-3}$	2.06	$1.13 \times 10^1$
554	$9.23 \times 10^{-4}$	$1.11 \times 10^{-3}$	$2.74 \times 10^{-3}$	1.20	2.96
1671	$3.46 \times 10^{-4}$	$1.75 \times 10^{-4}$	$1.21 \times 10^{-3}$	$5.05 \times 10^{-1}$	3.50
3848	$3.14 \times 10^{-5}$	$3.69 \times 10^{-5}$	$4.78 \times 10^{-4}$	1.18	$1.53 \times 10^1$
9925	$2.80 \times 10^{-6}$	$3.99 \times 10^{-6}$	$1.33 \times 10^{-4}$	1.42	$4.75 \times 10^1$
20687	$2.03 \times 10^{-6}$	$1.71 \times 10^{-6}$	$3.71 \times 10^{-5}$	$8.42 \times 10^{-1}$	$1.83 \times 10^1$
Uniform mesh refinement					
195	$8.80 \times 10^{-4}$	$1.81 \times 10^{-3}$	$9.96 \times 10^{-3}$	2.06	$1.13 \times 10^1$
657	$8.15 \times 10^{-4}$	$1.06 \times 10^{-3}$	$2.75 \times 10^{-3}$	1.30	3.37
2397	$2.26 \times 10^{-4}$	$1.55 \times 10^{-4}$	$1.16 \times 10^{-3}$	$6.88 \times 10^{-1}$	5.15
9141	$2.78 \times 10^{-5}$	$1.52 \times 10^{-5}$	$4.05 \times 10^{-4}$	$5.46 \times 10^{-1}$	$1.45 \times 10^1$
35685	$3.16 \times 10^{-7}$	$2.55 \times 10^{-6}$	$1.17 \times 10^{-4}$	8.09	$3.70 \times 10^2$
140997	$4.90 \times 10^{-7}$	$1.52 \times 10^{-6}$	$3.22 \times 10^{-5}$	3.10	$6.57 \times 10^1$

Table 2: Example 1: Degrees of freedom, true error, estimator and indices.

In Table 4, the values of the individual goal functionals and the combined goal functional are listed. These allow us to study the evolution of the individual goal functionals under mesh refinement for the different weights. For each weight combination, the reference  $J_c$  is obtained with the help of (20) and the values for  $J_{\text{drag}}(\hat{U})$  and  $J_2(\hat{u})$  listed in Table 1. This study is important insofar as we only control  $J_c$  via the adjoint problem in our multigoal framework, but not directly the individual goals.

$\omega_1$	$\omega_2$	Dofs	$ J_c(\hat{U}) - J_c(\hat{U}_h) $	$ \eta_h $	$\sum_i  \eta_i $	$I_{\text{eff}}$	$I_{\text{ind}}$
0.00	1.00	195	$6.20 \times 10^{-4}$	0.00	0.00	0.00	0.00
0.25	0.75	195	$1.30 \times 10^{-4}$	$9.04 \times 10^{-4}$	$4.98 \times 10^{-3}$	6.96	$3.84 \times 10^1$
0.25	0.75	554	$6.18 \times 10^{-4}$	$5.56 \times 10^{-4}$	$1.37 \times 10^{-3}$	$8.99 \times 10^{-1}$	2.21
0.25	0.75	1671	$3.19 \times 10^{-4}$	$8.75 \times 10^{-5}$	$6.05 \times 10^{-4}$	$2.74 \times 10^{-1}$	1.89
0.25	0.75	3848	$1.89 \times 10^{-5}$	$2.45 \times 10^{-5}$	$2.96 \times 10^{-4}$	1.29	$1.56 \times 10^1$
0.25	0.75	9448	$5.03 \times 10^{-6}$	$5.87 \times 10^{-6}$	$7.91 \times 10^{-5}$	1.17	$1.57 \times 10^1$
0.25	0.75	23303	$3.00 \times 10^{-7}$	$1.84 \times 10^{-6}$	$2.21 \times 10^{-5}$	6.12	$7.36 \times 10^1$
0.75	0.25	195	$1.63 \times 10^{-3}$	$2.71 \times 10^{-3}$	$1.49 \times 10^{-2}$	1.66	9.17
0.75	0.25	554	$1.23 \times 10^{-3}$	$1.67 \times 10^{-3}$	$4.10 \times 10^{-3}$	1.36	3.34
0.75	0.25	1671	$3.73 \times 10^{-4}$	$2.63 \times 10^{-4}$	$1.82 \times 10^{-3}$	$7.04 \times 10^{-1}$	4.87
0.75	0.25	3848	$4.38 \times 10^{-5}$	$4.94 \times 10^{-5}$	$6.62 \times 10^{-4}$	1.13	$1.51 \times 10^1$
0.75	0.25	9865	$1.07 \times 10^{-5}$	$1.38 \times 10^{-6}$	$1.89 \times 10^{-4}$	$1.29 \times 10^{-1}$	$1.77 \times 10^1$
0.75	0.25	20512	$1.15 \times 10^{-6}$	$1.07 \times 10^{-6}$	$5.33 \times 10^{-5}$	$9.32 \times 10^{-1}$	$4.63 \times 10^1$
1.00	0.00	195	$2.38 \times 10^{-3}$	$3.62 \times 10^{-3}$	$1.99 \times 10^{-2}$	1.52	8.37
1.00	0.00	554	$1.53 \times 10^{-3}$	$2.22 \times 10^{-3}$	$5.47 \times 10^{-3}$	1.45	3.57
1.00	0.00	1671	$4.00 \times 10^{-4}$	$3.50 \times 10^{-4}$	$2.42 \times 10^{-3}$	$8.75 \times 10^{-1}$	6.05
1.00	0.00	3848	$5.62 \times 10^{-5}$	$6.18 \times 10^{-5}$	$8.61 \times 10^{-4}$	1.10	$1.53 \times 10^1$
1.00	0.00	9797	$1.66 \times 10^{-6}$	$1.31 \times 10^{-6}$	$2.46 \times 10^{-4}$	$7.88 \times 10^{-1}$	$1.48 \times 10^2$
1.00	0.00	18985	$2.29 \times 10^{-6}$	$5.09 \times 10^{-7}$	$7.11 \times 10^{-5}$	$2.23 \times 10^{-1}$	$3.11 \times 10^1$

Table 3: Example 1: Degrees of freedom, true error, estimator and indices for different weights  $\omega_1, \omega_2$ . For each weight combination, the reference  $J_c$  is obtained with the help of (20) and the values for  $J_{\text{drag}}(\hat{U})$  and  $J_2(\hat{u})$  listed in Table 1.

In Figure 1 the primal solution is shown with the adaptively refined mesh. Refinements with respect to both goal functionals can be observed. In Figure 2, the displacement fields are displayed. Afterward, in Figure 3, the adjoint solutions of the velocities are shown. The overflow velocity boundary condition introduces pressure singularities in both upper corners. We also notice that at the boundary points where the FSI interface intersects, different boundary and interface conditions interact, which may also lead to a slight degeneration of the effectivity indices.

$\omega_1$	$\omega_2$	Dofs	$J_c(\hat{U})$	$J_{\text{drag}}(\hat{U})$	$J_2(\hat{U})$
0.00	1.00	195	$-4.07 \times 10^{-3}$	$-9.59 \times 10^{-2}$	$-4.07 \times 10^{-3}$
0.25	0.75	195	$-2.70 \times 10^{-2}$	$-9.59 \times 10^{-2}$	$-4.07 \times 10^{-3}$
0.25	0.75	554	$-2.63 \times 10^{-2}$	$-9.20 \times 10^{-2}$	$-4.38 \times 10^{-3}$
0.25	0.75	1671	$-2.66 \times 10^{-2}$	$-9.31 \times 10^{-2}$	$-4.40 \times 10^{-3}$
0.25	0.75	3848	$-2.69 \times 10^{-2}$	$-9.35 \times 10^{-2}$	$-4.68 \times 10^{-3}$
0.25	0.75	9448	$-2.69 \times 10^{-2}$	$-9.35 \times 10^{-2}$	$-4.68 \times 10^{-3}$
0.25	0.75	23303	$-2.69 \times 10^{-2}$	$-9.35 \times 10^{-2}$	$-4.69 \times 10^{-3}$
0.75	0.25	195	$-7.30 \times 10^{-2}$	$-9.59 \times 10^{-2}$	$-4.07 \times 10^{-3}$
0.75	0.25	554	$-7.01 \times 10^{-2}$	$-9.20 \times 10^{-2}$	$-4.38 \times 10^{-3}$
0.75	0.25	1671	$-7.10 \times 10^{-2}$	$-9.31 \times 10^{-2}$	$-4.40 \times 10^{-3}$
0.75	0.25	3848	$-7.13 \times 10^{-2}$	$-9.35 \times 10^{-2}$	$-4.68 \times 10^{-3}$
0.75	0.25	9865	$-7.13 \times 10^{-2}$	$-9.35 \times 10^{-2}$	$-4.68 \times 10^{-3}$
0.75	0.25	20512	$-7.13 \times 10^{-2}$	$-9.35 \times 10^{-2}$	$-4.69 \times 10^{-3}$
1.00	0.00	195	$-9.59 \times 10^{-2}$	$-9.59 \times 10^{-2}$	$-4.07 \times 10^{-3}$
1.00	0.00	554	$-9.20 \times 10^{-2}$	$-9.20 \times 10^{-2}$	$-4.38 \times 10^{-3}$
1.00	0.00	1671	$-9.31 \times 10^{-2}$	$-9.31 \times 10^{-2}$	$-4.40 \times 10^{-3}$
1.00	0.00	3848	$-9.35 \times 10^{-2}$	$-9.35 \times 10^{-2}$	$-4.68 \times 10^{-3}$
1.00	0.00	9797	$-9.35 \times 10^{-2}$	$-9.35 \times 10^{-2}$	$-4.68 \times 10^{-3}$
1.00	0.00	18985	$-9.35 \times 10^{-2}$	$-9.35 \times 10^{-2}$	$-4.69 \times 10^{-3}$

Table 4: Example 1: Actual values for the individual goals and combined goal functional.

## 5.2 Example 2: elastic bar in a chamber

This second configuration is taken from [45]. Here, the flow is driven by a pressure difference. This configuration is challenging for the ALE transformation because a higher inflow pressure yields higher fluid flow and will cause the elastic beam to close the small upper channel. Consequently, both the adjoint equation and the mesh motion technique play important roles.

**Configuration** The geometrical data is sketched in [45, Fig. 5.1, right subfigure] and also in the numerical results in Figure 4.

**Boundary conditions** On the outer boundary  $\partial\hat{\Omega}$  we work with homogeneous Dirichlet conditions of the displacements. On the left inflow boundary  $\partial\hat{\Omega}_{\text{left}}$  and right small channel outflow  $\partial\hat{\Omega}_{\text{right}}$  pressure conditions are prescribed:

$$\begin{aligned}\hat{g} &= 0.2I - \hat{\rho}_f \nu_f \hat{J}(\hat{F}^{-T} \hat{\nabla} \hat{v}_f^T \hat{n}_f) \hat{F}^{-T} \quad \text{on } \hat{\Gamma}_{\text{left}}, \\ \hat{g} &= -\hat{\rho}_f \nu_f \hat{J}(\hat{F}^{-T} \hat{\nabla} \hat{v}_f^T \hat{n}_f) \hat{F}^{-T} \quad \text{on } \hat{\Gamma}_{\text{right}},\end{aligned}$$

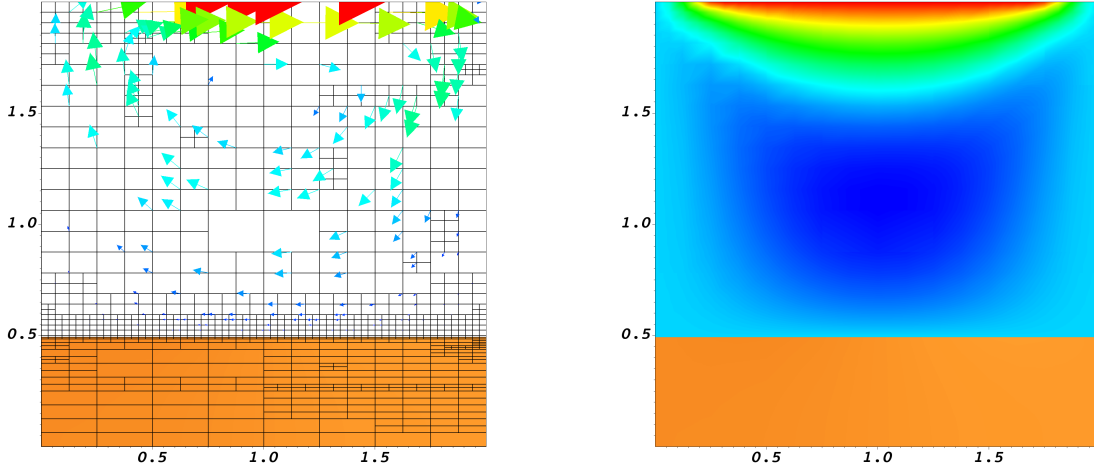


Figure 1: Example 1: Left: adaptive mesh and vector plot. We observe adaptive mesh refinement along the FSI interface and also around the point value evaluation of  $J_2(\hat{u}) := \hat{u}(1.5, 0.25)$ . Right: pseudocolor plot of  $\hat{u}_x$ . The lower brown part shows the elastic solid domain  $\hat{\Omega}_s$ .

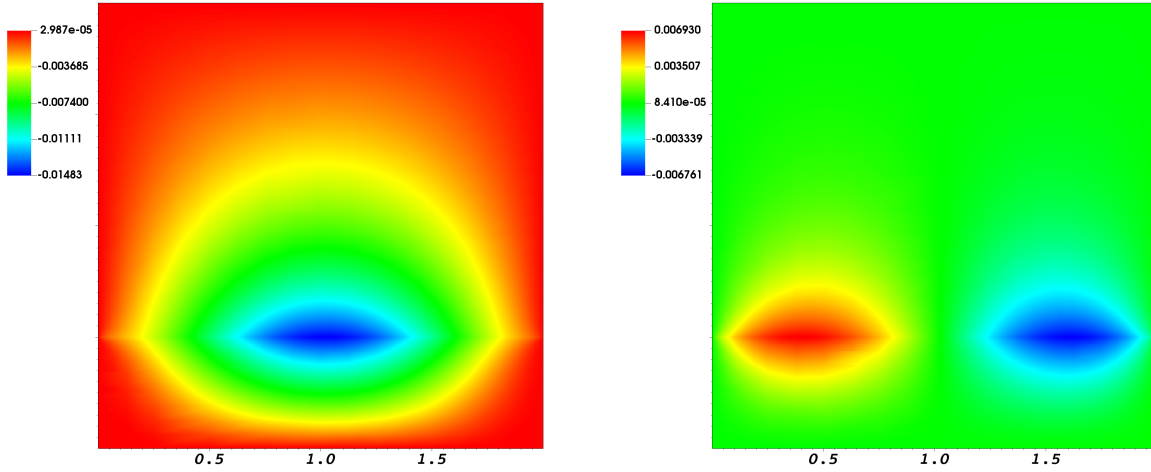


Figure 2: Example 1: Left and right: pseudocolor plots of the primal displacement solutions  $\hat{u}_x$  and  $\hat{u}_y$ , respectively.

where  $I$  is the identity matrix in  $\mathbb{R}^{2 \times 2}$ . This means that we prescribe a pressure of 0.2 Pa on the left inflow part  $\hat{\Gamma}_{\text{left}}$  and zero pressure on the small channel outlet  $\hat{\Gamma}_{\text{right}}$ . The second term is a correction term due to the symmetric fluid stress tensor due to the so-called do-nothing condition [36]. On the remaining outer boundaries, we prescribe  $\hat{v} = 0$  (homogeneous Dirichlet conditions).

**Parameters** We use the fluid density  $\varrho_f = 1000 \text{ kgm}^{-3}$  and kinematic viscosity  $\nu_f = 0.001 \text{ m}^2\text{s}^{-1}$ . The elastic solid is characterized by the density  $\varrho_s = 1000 \text{ kgm}^{-3}$  and Poisson's ratio  $\nu_s = 0.4$ . Furthermore, we use the Lamé coefficient  $\mu_s = 500 \text{ kgm}^{-1}\text{s}^{-2}$ .

**Goals** The combined functional consists of a line integral evaluation  $J_{\text{drag}} := F_D$  (see definition below (21)) and a point evaluation  $J_2(\hat{p}) = \hat{p}(2.0, 0.5)$  and reads

$$J_c(\hat{U}) = w_1 J_{\text{drag}}(\hat{U}) + w_2 J_2(\hat{p}).$$

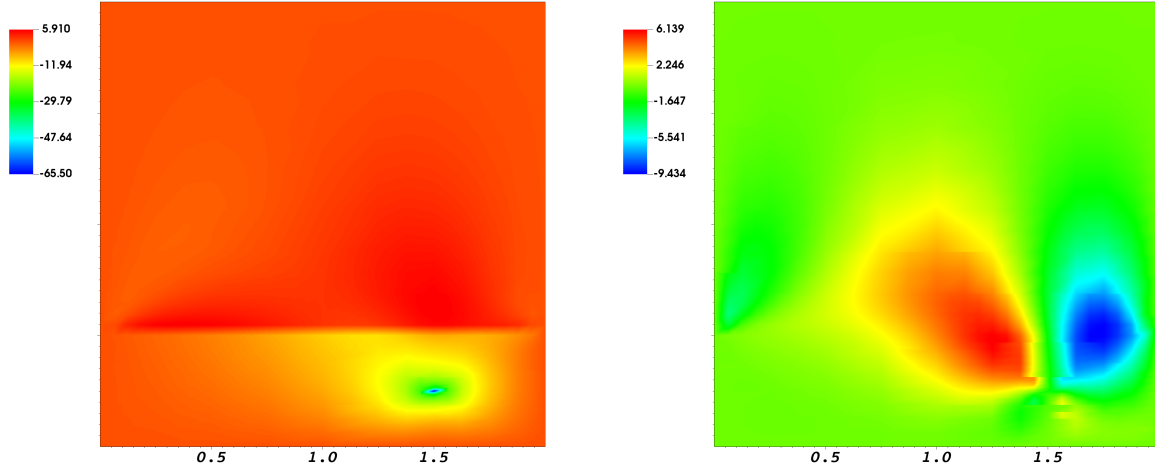


Figure 3: Example 1: Left and right: pseudocolor plots of the adjoint solutions  $z^{\hat{v}_x}$  and  $z^{\hat{v}_y}$ , respectively.

The weights are  $w_1, w_2 \in \mathbb{R}$  and  $\omega_1 = \omega_2 = 1$ . We recall that  $\hat{U} := (\hat{v}, \hat{u}, \hat{p})$ . The reference value is computed on a sufficiently refined mesh:

$$J_c(\hat{U}) = 2.70728 \times 10^{-1}.$$

**Results and discussion** Figures 4 and 5 display the adaptively refined mesh, the elastic bar, the flow field and the adjoint displacement solutions. The adjoint solutions clearly indicate a strong influence at the tip of the elastic bar and the small channel.

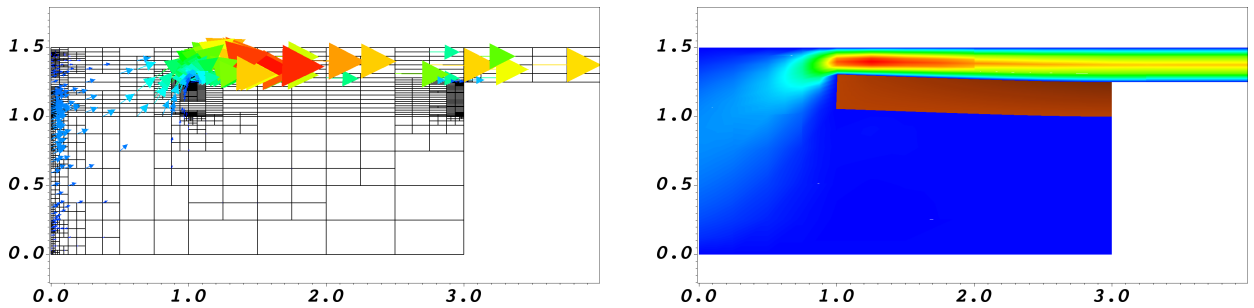


Figure 4: Example 2: locally refined mesh with vector plot of flow field (left) and flow field with elastic solid (brown) in the deformed configuration  $\Omega$ .

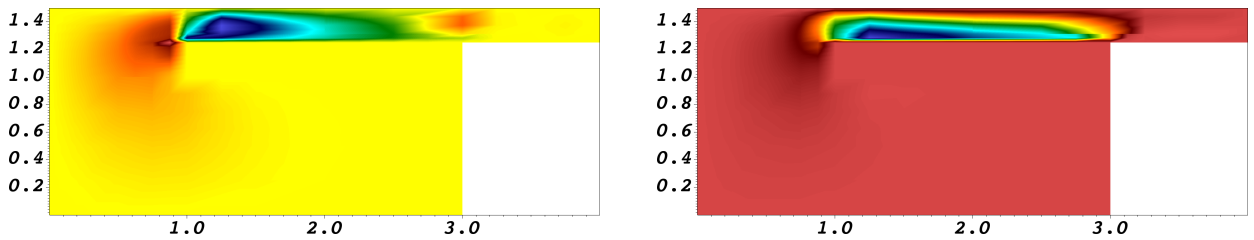


Figure 5: Example 2: adjoint displacement solutions  $\hat{z}^{u_x}$  and  $\hat{z}^{u_y}$ .

The final values of the two goal functionals and the combined goal functional are provided in Table 5.



Drag	$7.082 \times 10^{-2}$
Pressure	$2.000 \times 10^{-1}$
$J_c$	$2.708 \times 10^{-1}$

Table 5: Example 2: Final values of goal functionals.

The true error, estimated error  $\eta_h$  and corresponding indices behave as given in Table 6. Again, we compare adaptive and uniform mesh refinement. On refinement level  $l = 4$  we need approximately 10 times more degrees of freedom to achieve a comparable true error. However, uniform mesh refinement yields better values in the estimator, which confirms our previous interpretation that adaptive refinement is sensitive in terms of the error estimator.

Level $l$	Dofs	$ J_c(\hat{U}) - J_c(\hat{U}_h) $	$ \eta_h $	$\sum_i  \eta_i $	$I_{\text{eff}}$	$I_{\text{ind}}$
1	2125	$8.48 \times 10^{-4}$	$5.59 \times 10^{-4}$	$9.57 \times 10^{-4}$	$6.59 \times 10^{-1}$	1.13
2	5508	$3.49 \times 10^{-4}$	$8.23 \times 10^{-5}$	$5.79 \times 10^{-4}$	$2.36 \times 10^{-1}$	1.66
3	10674	$1.39 \times 10^{-4}$	$1.74 \times 10^{-3}$	$2.09 \times 10^{-3}$	$1.25 \times 10^1$	$1.50 \times 10^1$
4	16383	$4.62 \times 10^{-5}$	$1.15 \times 10^{-3}$	$1.36 \times 10^{-3}$	$2.49 \times 10^1$	$2.94 \times 10^1$
5	25994	$2.89 \times 10^{-6}$	$2.16 \times 10^{-3}$	$2.30 \times 10^{-3}$	$7.47 \times 10^2$	$7.94 \times 10^2$
6	36596	$9.80 \times 10^{-5}$	$1.34 \times 10^{-3}$	$1.47 \times 10^{-3}$	$1.37 \times 10^1$	$1.50 \times 10^1$
Uniform mesh refinement						
1	2125	$8.48 \times 10^{-4}$	$5.59 \times 10^{-4}$	$9.57 \times 10^{-4}$	$6.59 \times 10^{-1}$	1.13
2	8053	$3.50 \times 10^{-4}$	$1.95 \times 10^{-4}$	$4.29 \times 10^{-4}$	$5.57 \times 10^{-1}$	1.22
3	31333	$1.36 \times 10^{-4}$	$6.38 \times 10^{-5}$	$2.16 \times 10^{-4}$	$4.69 \times 10^{-1}$	1.59
4	123589	$4.14 \times 10^{-5}$	$1.71 \times 10^{-5}$	$1.16 \times 10^{-4}$	$4.12 \times 10^{-1}$	2.80

Table 6: Example 2: Degrees of freedom, true error, estimator and indices.

We observe sufficient decrease in the true error and estimated error as well as the indicator index. However, there is a large difference of about one order of magnitude resulting in an overestimation of both the effectivity and indicator indices. The reason for this is the specific setting, which is very sensitive to the ALE transformation and also to the relatively large influence of the adjoint.

### 5.3 Example 3: FSI-1 benchmark

This configuration is taken from [37]. Our own results using uniform mesh refinement are provided in [52, 44]. The extension to multiple goal functionals is novel.

**Configuration** The computational domain has length  $L = 2.5$  m and height  $H = 0.41$  m. The circle center is positioned at  $C = (0.2 \text{ m}, 0.2 \text{ m})$  with radius  $r = 0.05$  m. The elastic beam has length  $l = 0.35$  m and height  $h = 0.02$  m. The right lower end is positioned at  $(0.6 \text{ m}, 0.19 \text{ m})$ , and the left end is attached to the circle.

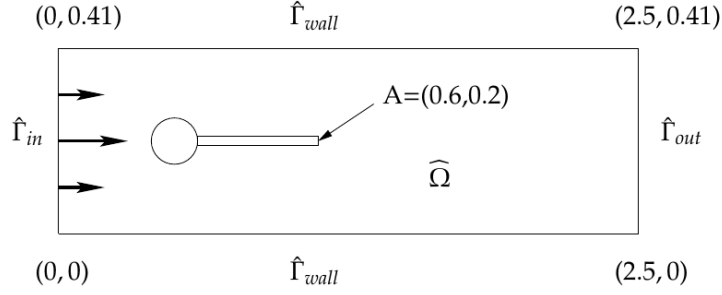


Figure 6: Flow around cylinder with elastic beam with circle-center  $C = (0.2, 0.2)$  and radius  $r = 0.05$ .

Control points  $A(t)$  (with  $A(0) = (0.6, 0.2)$ ) are fixed at the trailing edge of the structure, measuring  $x$ - and  $y$ -deflections of the beam.

**Boundary conditions** A parabolic inflow velocity profile is given on  $\hat{\Gamma}_{in}$  by

$$v_f(0, y) = 1.5\bar{U} \frac{4y(H-y)}{H^2}, \quad \bar{U} = 0.2 \text{ ms}^{-1}.$$

On the outlet  $\hat{\Gamma}_{out}$  the ‘do-nothing’ outflow condition [36] is imposed which leads to zero mean value of the pressure at this part of the boundary. The displacements are fixed (homogeneous Dirichlet conditions) around the outer boundary and the cylinder. On  $\hat{\Gamma}_{wall}$  no-slip conditions for flow (homogeneous Dirichlet for velocities  $\hat{v}$ ) are prescribed.

**Parameters** We use the fluid density  $\rho_f = 1000 \text{ kgm}^{-3}$  and kinematic viscosity  $\nu_f = 0.001 \text{ m}^2\text{s}^{-1}$ . The elastic solid is characterized by the density  $\rho_s = 100 \text{ kgm}^{-3}$  and Poisson’s ratio  $\nu_s = 0.4$ . Furthermore, we use the Lamé coefficient  $\mu_s = 0.5 \times 10^6 \text{ kgm}^{-1}\text{s}^{-2}$ .

**Quantities of interest of the original benchmark problem** In the benchmark configuration [37] four quantities of interest were evaluated:

- 1)  $x$ - and  $y$ -deflection of the beam at  $A(t)$ .
- 2) The forces exerted by the fluid on the whole body, i.e., drag force  $F_D$  and lift force  $F_L$  on the rigid cylinder and the elastic beam. They form a closed path in which the forces can be computed with the help of line integration. The formula is evaluated on the fixed reference domain  $\hat{\Omega}$  and reads:

$$(F_D, F_L) = \int_{\hat{S}} \hat{J} \hat{\sigma}_{all} \hat{F}^{-T} \cdot \hat{n} d\hat{s} = \int_{\hat{S}(\text{circle})} \hat{J} \hat{\sigma}_f \hat{F}^{-T} \cdot \hat{n}_f d\hat{s} + \int_{\hat{S}(\text{beam})} \hat{J} \hat{\sigma}_f \hat{F}^{-T} \cdot \hat{n}_f d\hat{s}. \quad (21)$$

**Goals** We consider three goal functionals simultaneously. The previous benchmark quantities of interest all yield local refinements around the FSI interface, when goal-oriented error control is employed. In order to highlight more clearly that three really distinct functionals can be controlled, we choose (1) the above drag functional, (2) away from the FSI interface, a pressure point evaluation in

$J_2(\hat{p}) := \hat{p}(1.5, 0.3)$ , and (3) the flux evaluation on the boundary  $\hat{\Gamma}_{\text{out}}$ , i.e.,  $\int_{\hat{\Gamma}_{\text{out}}} \hat{v}_f \cdot \hat{n} ds$ . Thus, the combined functional reads

$$J_c(\hat{U}) = w_1 J_{\text{drag}}(\hat{U}) + w_2 J_2(\hat{p}) + w_3 J_3(\hat{v}).$$

The weights are  $w_1, w_2, w_3 \in \mathbb{R}$ ,  $w_1 = w_2 = w_3 = 1$ , and we recall that  $\hat{U} := (\hat{v}, \hat{u}, \hat{p})$ . The reference value is computed on a sufficiently refined mesh:

$$J_c(\hat{U}) = 3.12053 \times 10^1.$$

**Results and discussion** In Figure 7, the final adaptive mesh and primal solution fields are shown. All adjoint solution fields are shown in Figure 8.

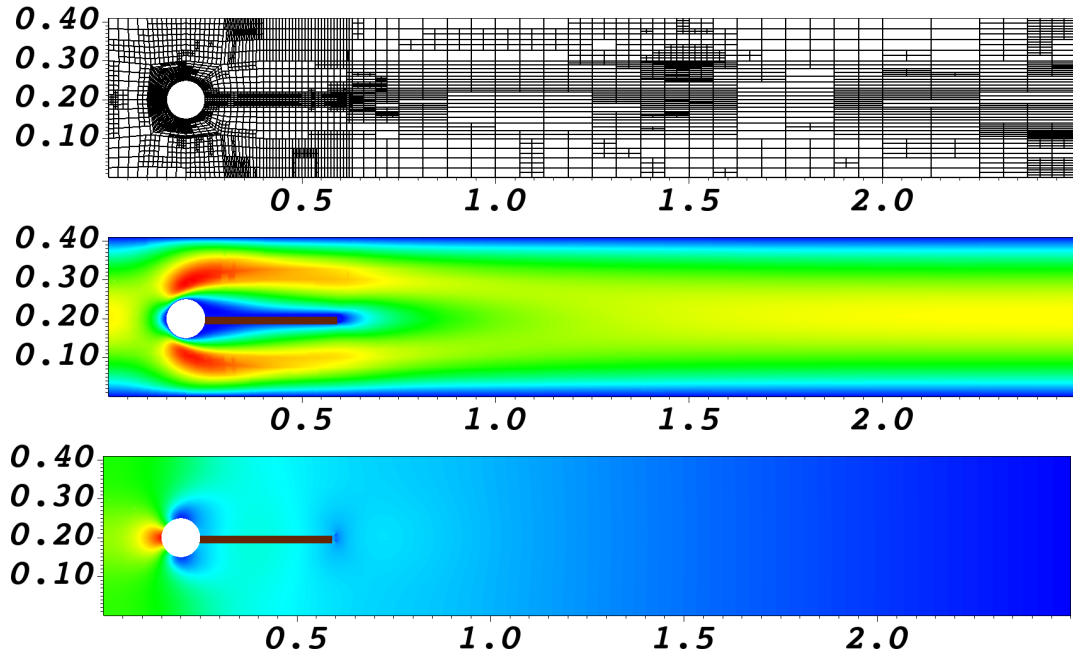


Figure 7: From top to bottom: adaptively refined mesh,  $\hat{v}_s$  velocity field, and the pressure field after three adaptive refinement steps. The elastic beam is colored in blue in the middle figure. In the top figure, we observe adaptive mesh refinement mainly around the interface between the elastic beam and the surrounding fluid and also in the pressure point evaluation at  $J_2(\hat{p}) := \hat{p}(1.5, 0.3)$ .

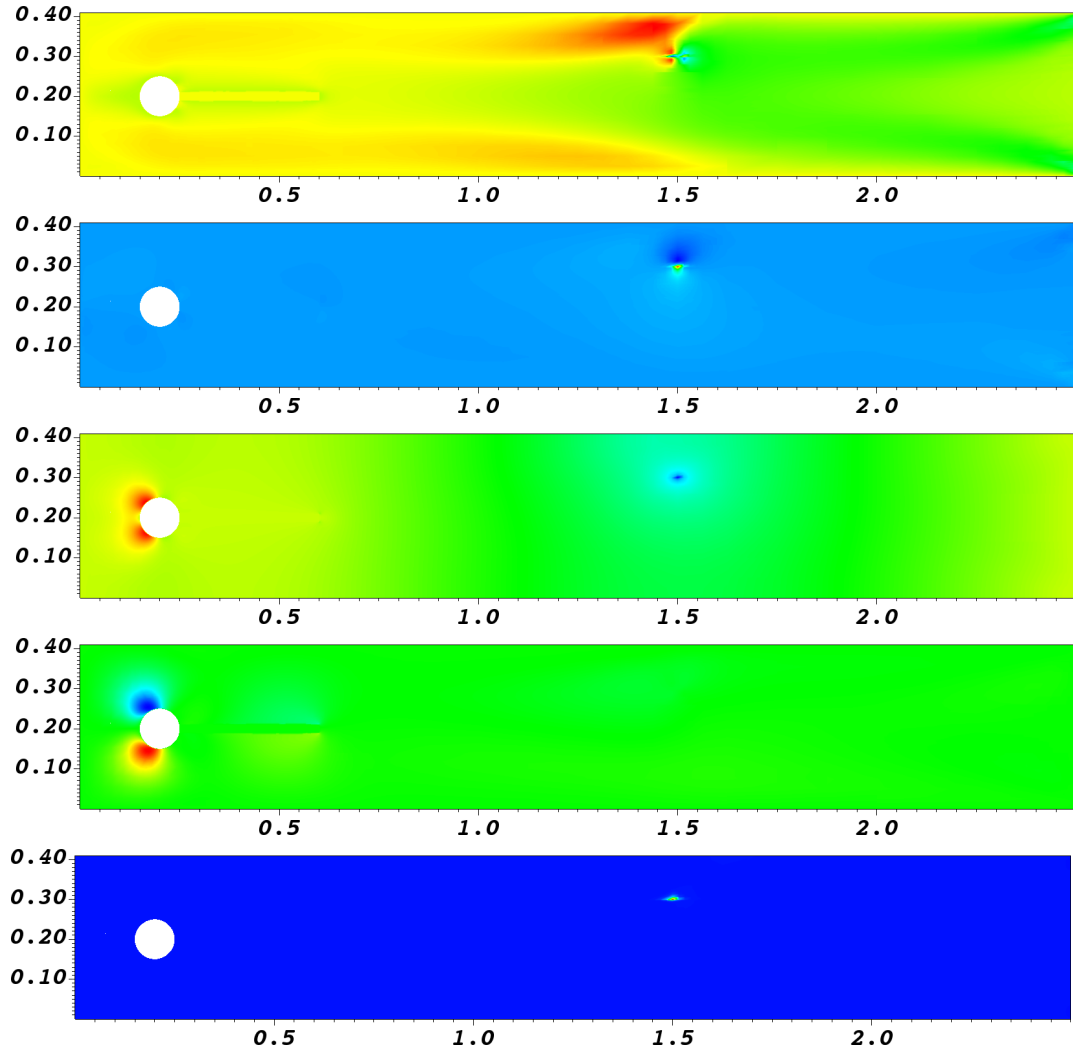


Figure 8: From top to bottom: adjoint solutions for  $\hat{z}^{\hat{v}_x}$ ,  $\hat{z}^{\hat{v}_y}$ ,  $\hat{z}^{\hat{u}_x}$ ,  $\hat{z}^{\hat{u}_y}$  and  $\hat{z}^{\hat{p}}$ .

Independently of the specific multi-goal framework, we first notice that the obtained FSI benchmark values agree well with the literature values [37, 52], see Table 7.

DisX	$2.266 \times 10^{-5}$
DisY	$8.200 \times 10^{-4}$
Drag	$1.535 \times 10^1$
Lift	$7.389 \times 10^{-1}$

Table 7: Example 3: Final values of  $x$ - and  $y$ -deflection of the beam at  $A(t)$ , drag, and lift.

The final drag, pressure value and flux values (multiple goal functionals) and the combined goal functional are given in Table 8.

Drag	$1.535 \times 10^1$
Pressure	$1.577 \times 10^1$
Flux	$8.200 \times 10^{-2}$
$J_c$	$3.120 \times 10^1$

Table 8: Example 3: Final values of the multigoal functionals.

With regard to our three goal functionals and error estimator, we obtained the results given in Table 9. Therein, at the second and third refinement levels we need two and four times more degrees of freedom, respectively, to achieve comparable true errors and estimators, which shows that our adaptive multigoal scheme can achieve a significant reduction of computational cost.

Level $l$	Dofs	$ J_c(\hat{U}) - J_c(\hat{U}_h) $	$ \eta_h $	$\sum_i  \eta_i $	$I_{\text{eff}}$	$I_{\text{ind}}$
1	13310	$2.73 \times 10^{-1}$	$1.42 \times 10^{-1}$	$5.41 \times 10^{-1}$	0.520	1.98
2	27193	$7.87 \times 10^{-2}$	$4.46 \times 10^{-2}$	$1.69 \times 10^{-1}$	0.566	2.15
3	54893	$2.05 \times 10^{-2}$	$1.24 \times 10^{-2}$	$6.11 \times 10^{-2}$	0.607	2.98
4	109909	$5.35 \times 10^{-3}$	$4.42 \times 10^{-3}$	$2.88 \times 10^{-2}$	0.826	5.39
Uniform mesh refinement						
1	13310	$2.73 \times 10^{-1}$	$1.42 \times 10^{-1}$	$5.41 \times 10^{-1}$	0.520	1.98
2	52052	$7.48 \times 10^{-2}$	$4.52 \times 10^{-2}$	$1.60 \times 10^{-1}$	0.605	2.14
3	205832	$2.04 \times 10^{-2}$	$1.32 \times 10^{-2}$	$5.64 \times 10^{-2}$	0.649	2.76

Table 9: Example 3: Degrees of freedom, true error, estimator and indices.

Therein, we observe well that the estimated error decreases by two orders of magnitude and  $I_{\text{eff}}$  and  $I_{\text{ind}}$  show a nice behavior. In view of the complexity of the problem statement dealing with a nonlinear, coupled fluid-structure interaction system and only working with the primal error estimator, these are excellent results which show that the multigoal-technology performs well for this example.

## 6 Conclusions

In this work, we developed multigoal-oriented a posteriori error control for stationary fluid-structure interaction. Specifically, the simultaneous control of several quantities of interest for such multiphysics problems may be required in practical applications. The focus in this work was on prototype settings for verification of our proposed multigoal framework. Three numerical tests, namely an elastic lid-driven cavity, a chamber with elastic solid and the FSI-1 benchmark were adopted to study the performance of our methodology. Therein, the lid-driven cavity (Example 1) and the FSI-1 benchmark (Example 3) yield good error reductions, good estimators and therefore good effectivity indices. The resulting adaptive meshes localize well the different goal functionals. Moreover, different weights were investigated in Example 1. In Example 2, the error reductions are also good, but the effectivity index shows an overestimation of about one order magnitude. This test is somewhat challenging due to

the large solid displacement and the influence of the adjoint solution. Two (Examples 1 and 2) and three (Example 3) goal functionals were studied and the overall performance is excellent in view of the complexity of the governing fluid-structure interaction system. A future (challenging) extension is the development of a multigoal framework for time-dependent fluid-structure interaction problems.

## Acknowledgments

This work has been supported by the DAAD in the project ‘A new passage to India’ between the Leibniz University Hannover and IIT Indore. Furthermore, the second and last author are affiliated to the Cluster of Excellence PhoenixD (EXC 2122, Project ID 390833453). Moreover, the second author acknowledges support from the Austrian Science Fund (FWF) under the grant P-29181 ‘Goal-Oriented Error Control for Phase-Field Fracture Coupled to Multiphysics Problems’ at the beginning of this work in Linz. The third author is funded by the Deutsche Forschungsgemeinschaft (DFG, German Research Foundation) – SFB1463 – 434502799.

## References

- [1] A. Agouzal. On the saturation assumption and hierarchical a posteriori error estimator. *Comput. Methods Appl. Math.*, 2(2):125–131, 2002.
- [2] D. Arndt, W. Bangerth, T. C. Clevenger, D. Davydov, M. Fehling, D. Garcia-Sanchez, G. Harper, T. Heister, L. Heltai, M. Kronbichler, R. M. Kynch, M. Maier, J.-P. Pelteret, B. Turcksin, and D. Wells. The `deal.II` library, version 9.1. *Journal of Numerical Mathematics*, 27:203–213, 2019.
- [3] D. Arndt, W. Bangerth, D. Davydov, T. Heister, L. Heltai, M. Kronbichler, M. Maier, J.-P. Pelteret, B. Turcksin, and D. Wells. The `deal.ii` finite element library: Design, features, and insights. *Computers & Mathematics with Applications*, 2020.
- [4] I. Babuska and W. C. Rheinboldt. A-posteriori error estimates for the finite element method. *International Journal for Numerical Methods in Engineering*, 12(10):1597–1615, 1978.
- [5] W. Bangerth and R. Rannacher. *Adaptive Finite Element Methods for Differential Equations*. Birkhäuser, Lectures in Mathematics, ETH Zürich, 2003.
- [6] Y. Bazilevs, K. Takizawa, and T. Tezduyar. *Computational Fluid-Structure Interaction: Methods and Applications*. Wiley, 2013.
- [7] R. Becker and R. Rannacher. An optimal control approach to a posteriori error estimation in finite element methods. *Acta Numer.*, 10:1–102, 2001.
- [8] T. Bodnár, G. Galdi, and Š. Nečasová. *Fluid-Structure Interaction and Biomedical Applications*. Advances in Mathematical Fluid Mechanics. Springer Basel, 2014.
- [9] D. Braess. *Finite Elemente; Theorie, schnelle Löser und Anwendungen in der Elastizitätstheorie*. Springer-Verlag Berlin Heidelberg, 4., überarbeitete und erweiterte Auflage edition, 2007.

- [10] H.-J. Bungartz, M. Mehl, and M. Schäfer. *Fluid-Structure Interaction II: Modelling, Simulation, Optimization*. Lecture Notes in Computational Science and Engineering. Springer, 2010.
- [11] H.-J. Bungartz and M. Schäfer. *Fluid-Structure Interaction: Modelling, Simulation, Optimization*, volume 53 of *Lecture Notes in Computational Science and Engineering*. Springer, 2006.
- [12] G. F. Carey and J. T. Oden. *Finite Elements. Volume III. Computational Aspects*. The Texas Finite Element Series, Prentice-Hall, Inc., Englewood Cliffs, 1984.
- [13] P. G. Ciarlet. *Mathematical Elasticity. Volume 1: Three Dimensional Elasticity*. North-Holland, 1984.
- [14] P. G. Ciarlet. *Finite Element Method for Elliptic Problems*. Society for Industrial and Applied Mathematics, Philadelphia, PA, USA, 2002.
- [15] J. Donéa, P. Fasoli-Stella, and S. Giuliani. Lagrangian and Eulerian finite element techniques for transient fluid-structure interaction problems. In *Trans. 4th Int. Conf. on Structural Mechanics in Reactor Technology*, page Paper B1/2, 1977.
- [16] W. Dörfler and R. H. Nochetto. Small data oscillation implies the saturation assumption. *Numer. Math.*, 91(1):1–12, 2002.
- [17] T. Dunne. An Eulerian approach to fluid-structure interaction and goal-oriented mesh adaption. *Int. J. Numer. Methods in Fluids*, 51:1017–1039, 2006.
- [18] T. Dunne. *Adaptive Finite Element Approximation of Fluid-Structure Interaction Based on Eulerian and Arbitrary Lagrangian-Eulerian Variational Formulations*. PhD thesis, University of Heidelberg, 2007.
- [19] T. Dunne, T. Richter, and R. Rannacher. *Numerical simulation of fluid-structure interaction based on monolithic variational formulations*, pages 1–75. Contemporary Challenges in Mathematical Fluid Mechanics. Springer, World Scientific, Singapore, 2010.
- [20] B. Endtmayer. *Multi-goal oriented a posteriori error estimates for nonlinear partial differential equations*. PhD thesis, Johannes Kepler University Linz, 2021.
- [21] B. Endtmayer, U. Langer, I. Neitzel, T. Wick, and W. Wollner. Multigoal-oriented optimal control problems with nonlinear PDE constraints. *Computers & Mathematics with Applications*, 2020, doi: <https://doi.org/10.1016/j.camwa.2020.01.005>.
- [22] B. Endtmayer, U. Langer, and T. Wick. Multigoal-oriented error estimates for non-linear problems. *Journal of Numerical Mathematics*, 2018.
- [23] B. Endtmayer, U. Langer, and T. Wick. Two-Side a Posteriori Error Estimates for the Dual-Weighted Residual Method. *SIAM J. Sci. Comput.*, 42(1):A371–A394, 2020.

- [24] B. Endtmayer, U. Langer, and T. Wick. Reliability and efficiency of dwr-type a posteriori error estimates with smart sensitivity weight recovering. *Computational Methods in Applied Mathematics*, 21(2):351–371, 2021.
- [25] B. Endtmayer and T. Wick. A partition-of-unity dual-weighted residual approach for multi-objective goal functional error estimation applied to elliptic problems. *Computational Methods in Applied Mathematics*, 17(2):575–599, 2017.
- [26] L. Failer and T. Wick. Adaptive time-step control for nonlinear fluid-structure interaction. *Journal of Computational Physics*, 366:448 – 477, 2018.
- [27] P. Fick, E. Brummelen, and K. Zee. On the adjoint-consistent formulation of interface conditions in goal-oriented error estimation and adaptivity for fluid-structure interaction. *Computer Methods in Applied Mechanics and Engineering*, 199:3369–3385, 2010.
- [28] L. Formaggia and F. Nobile. A stability analysis for the arbitrary Lagrangian Eulerian formulation with finite elements. *East-West Journal of Numerical Mathematics*, 7:105 – 132, 1999.
- [29] L. Formaggia and F. Nobile. Stability analysis of second-order time accurate schemes for ALE-FEM. *Comp. Methods Appl. Mech. Engrg.*, 193(39-41):4097 – 4116, 2004.
- [30] L. Formaggia, A. Quarteroni, and A. Veneziani. *Cardiovascular Mathematics: Modeling and simulation of the circulatory system*. Springer-Verlag, Italia, Milano, 2009.
- [31] S. Frei, B. Holm, T. Richter, T. Wick, and H. Yang. *Fluid-structure interactions: Fluid-Structure Interaction: Modeling, Adaptive Discretisations and Solvers*. de Gruyter, 2017.
- [32] G. Galdi and R. Rannacher. *Fundamental Trends in Fluid-Structure Interaction*. World Scientific, 2010.
- [33] T. Grätsch and K.-J. Bathe. Goal-oriented error estimation in the analysis of fluid flows with structural interactions. *Comp. Methods Appl. Mech. Engrg.*, 195:5673–5684, 2006.
- [34] R. Hartmann. Multitarget error estimation and adaptivity in aerodynamic flow simulations. *SIAM Journal on Scientific Computing*, 31(1):708–731, 2008.
- [35] R. Hartmann and P. Houston. Goal-oriented a posteriori error estimation for multiple target functionals. In T. Hou and E. Tadmor, editors, *Hyperbolic Problems: Theory, Numerics, Applications*, pages 579–588. Springer Berlin Heidelberg, 2003.
- [36] J. G. Heywood, R. Rannacher, and S. Turek. Artificial boundaries and flux and pressure conditions for the incompressible Navier-Stokes equations. *International Journal of Numerical Methods in Fluids*, 22:325–352, 1996.
- [37] J. Hron and S. Turek. *Proposal for numerical benchmarking of fluid-structure interaction between an elastic object and laminar incompressible flow*, volume 53, pages 146 – 170. Springer-Verlag, 2006.



- [38] T. Hughes, W. Liu, and T. Zimmermann. Lagrangian-Eulerian finite element formulation for incompressible viscous flows. *Comput. Methods Appl. Mech. Engrg.*, 29:329–349, 1981.
- [39] K. Kergrene, S. Prudhomme, L. Chamoin, and M. Laforest. A new goal-oriented formulation of the finite element method. *Comput. Methods Appl. Mech. Engrg.*, 327:256–276, 2017.
- [40] D. Pardo. Multigoal-oriented adaptivity for hp-finite element methods. *Procedia Computer Science*, 1(1):1953 – 1961, 2010.
- [41] R. Rannacher and J. Vihharev. Adaptive finite element analysis of nonlinear problems: balancing of discretization and iteration errors. *J. Numer. Math.*, 21(1):23–61, 2013.
- [42] T. Richter. Goal-oriented error estimation for fluid–structure interaction problems. *Computer Methods in Applied Mechanics and Engineering*, 223-224:28 – 42, 2012.
- [43] T. Richter. *Fluid-structure interactions: models, analysis, and finite elements*. Springer, 2017.
- [44] T. Richter and T. Wick. Finite elements for fluid-structure interaction in ALE and fully Eulerian coordinates. *Comp. Methods Appl. Mech. Engrg.*, 199:2633–2642, 2010.
- [45] T. Richter and T. Wick. Optimal control and parameter estimation for stationary fluid-structure interaction. *SIAM J. Sci. Comput.*, 35(5):B1085–B1104, 2013.
- [46] T. Richter and T. Wick. Variational localizations of the dual weighted residual estimator. *J. Comput. Appl. Math.*, 279:192–208, 2015.
- [47] A. Shamanskiy and B. Simeon. Mesh moving techniques in fluid-structure interaction: robustness, accumulated distortion and computational efficiency. *Comput. Mech.*, 67(2):583–600, 2021.
- [48] K. Stein, T. Tezduyar, and R. Benney. Mesh moving techniques for fluid-structure interactions with large displacements. *J. Appl. Mech.*, 70:58–63, 2003.
- [49] E. H. van Brummelen, S. Zhuk, and G. van Zwieten. Worst-case multi-objective error estimation and adaptivity. *Computer Methods in Applied Mechanics and Engineering*, 313:723–743, 2017.
- [50] K. van der Zee, E. H. van Brummelen, I. Akkerman, and R. de Borst. Goal-oriented error estimation and adaptivity for fluid–structure interaction using exact linearized adjoints. *Computer Methods in Applied Mechanics and Engineering*, 200(37):2738–2757, 2011.
- [51] T. Wick. Fluid-structure interactions using different mesh motion techniques. *Computers and Structures*, 89(13-14):1456–1467, 2011.
- [52] T. Wick. Solving monolithic fluid-structure interaction problems in arbitrary Lagrangian Eulerian coordinates with the deal.II library. *Archive of Numerical Software*, 1:1–19, 2013.
- [53] T. Wick. *Multiphysics Phase-Field Fracture: Modeling, Adaptive Discretizations, and Solvers*. De Gruyter, Berlin, Boston, 2020.

- [54] T. Wick. Adjoint-based methods for optimization and goal-oriented error control applied to fluid-structure interaction: implementation of a partition-of-unity dual-weighted residual estimator for stationary forward FSI problems in deal.II, 2021. arXiv 2105.11145.
- [55] J. Wloka. *Partial differential equations*. Cambridge University Press, 1987.